Journal of Alloys and Compounds 811 (2019) 152024

Contents lists available at ScienceDirect

Journal of Alloys and Compounds

journal homepage: http://www.elsevier.com/locate/jalcom

Tailoring the micromorphology of the as-cast Mg–Sn–In alloys to corrosion-resistant microstructures via adjusting In concentration

Ming Yin [a, c], Lifeng Hou [a, c, **], Xiaoda Liu [a, c], Zhiwei Wang [a, c], Baosheng Liu [b, c], Jianwen Jia [a, c], Shaohua Zhang [a, c], Yinghui Wei [a, b, c, *]

[a] College of Materials Science and Engineering, Taiyuan University of Technology, Taiyuan, 030024, Shanxi, China
[b] College of Materials Science and Engineering, Taiyuan University of Science and Technology, Taiyuan, 030024, Shanxi, China
[c] Corrosion and Protection Engineering Technology Research Center of Shanxi Province, Taiyuan, 030024, Shanxi, China

ARTICLE INFO

Article history:
Received 20 June 2019
Received in revised form
24 August 2019
Accepted 26 August 2019
Available online 27 August 2019

Keywords:
Mg-Sn alloy
Microstructure
SEM
Corrosion behavior

ABSTRACT

The initiation and propagation of corrosion was characterized and evaluated by means of morphology observation, composition analyses and electrochemical tests. It was found that the microstructures of as-cast Mg–Sn–In alloys could be adjusted by varying the In concentration. Moreover, activation and inhibition mechanisms are present in the Mg–Sn–In alloys, which cause the compactness of the corrosion layer to be various. The anti-corrosion of an as-cast Mg–1Sn–2In alloy was obtained by adjusting the concentration of In. The Mg–1Sn–2In alloy possessed a "flower"-like morphology that blocked corrosion propagation and formd a compact corrosion film. In this way, a method of adjusting the microstructures and the compactness of the corrosion layer by addition of a small amount of In is proposed, and the superiority of its microstructure confirmed.

1. Introduction

Magnesium (Mg) alloys exhibit excellent characteristics such as low density, high strength-to-weight ratio, environmental friendliness and good elastic modulus, making them widely applicable in aerospace, electronics and automotive industries [1–3]. However, a long-term obstacle to their adoption is vulnerability to severe corrosion, which curtails their shelf-life [4]. This predicament is mainly because the $Mg(OH)_2$ film formed by oxidation of Mg in air is porous and non-protected, especially in humid environments [5–7]. Customarily, mitigation methods include: metallurgical alloying [8–10], chemical conversion coating [11–14], electrochemical plating [15,16], anodic oxidation [17] or use of additive corrosion inhibitors [18]. Unfortunately, in addition to alloying, the aforementioned methods are cumbersome and inevitably produce chemical wastes to some extent. Mg alloying is a favorable approach that can slow down corrosion effectively.

In recent years, several scholars have focused on the addition of various elements to Mg alloys [19–23]. The diversity of corrosion mechanisms corresponds to the different elements used in the alloys, and five main methods have been described. First, by altering the volume fraction and distribution of the $Mg_{17}Al_{12}$ phases, the corrosion mechanism of phases with a network-blocking effect or dispersed phases having an accelerated corrosion effect was proposed by Song et al. [24]. The effects of Ge on Mg–Al alloys [19] and Ca on Mg–Al–Mn alloys [25] have also been included in alloying elements with similar corrosion mechanisms. Second, scholars [1,25–27] have added elements such as Mn, Ti and Zr combined with impurities, which increases the purity of alloys and reduces corrosion significantly. Moreover, improving the corrosion resistance of alloys by refining grains has been confirmed by many researchers [22,28,29]. Third, rare-earth elements [2,30–33] can refine the microstructure, thereby facilitating formation of a more uniform β-$Mg_{17}Al_{12}$ phase network. Fourth, the corrosion resistance of Mg is improved significantly by using a trace amount of alloyed arsenic (As). Nick et al. [34] proposed that the alloying addition of As could interfere with recombination with the hydrogen atom through a mechanism of cathodic poisoning, which can reduce cathodic kinetics and improve the corrosion resistance of Mg significantly. Fifth, the surface film can be altered by adding elements [35,36]. Hou et al. [36] studied the dynamics of formation of a Li-rich surface film on Mg–Li alloys, and found that Li_2CO_3

* Corresponding author. College of Materials Science and Engineering, Taiyuan University of Technology, Taiyuan, 030024, Shanxi, China.
** Corresponding author. Corrosion and Protection Engineering Technology Research Center of Shanxi Province, Taiyuan, 030024, Shanxi, China.
E-mail addresses: houlifeng78@126.com (L. Hou), yhwei_tyut@126.com (Y. Wei).

https://doi.org/10.1016/j.jallcom.2019.152024
0925-8388/

protected the film from corrosion in a stable fashion. This method of altering the surface film by adding Li has achieved good results.

The corrosion resistance of Mg-based alloys is highly dependent on their microstructures and the degree of compactness of the formed films. Hence, some alloying elements could control the microstructures and ameliorate the compactness of the corrosion layers of Mg alloys simultaneously. In addition, if it is desired to utilize segregation under certain circumstances (e.g., a Mg−Sn-based anode battery), the microstructures of alloys are "tailored" to enhance corrosion resistance as required. Mg−Sn−In alloys were chosen as the research subjects to confirm this assumption because as-cast Mg−Sn alloys show dendrite segregation under certain conditions (the solid solubility of Sn in Mg is approximately 0.45% at 200 °C), which can provide commendable samples of the microstructures. Indium (In) has high solid solubility in α-Mg (53.5 wt %), so the secondary phases cannot be traced [37]. Therefore, In was selected to alter the microstructures of Mg−Sn alloys (excluding the influence of secondary phases on corrosion). Simultaneously, a porous film of magnesium hydroxide ($Mg(OH)_2$) can be filled by the oxidation products formed by corrosion of this element. To affirm this conception, the effects of a range of In concentrations of Mg−Sn−In alloys on microstructures and anti-corrosion were investigated, the initiation and propagation of corrosion discussed, and the roles of elements in the corrosion mechanism elucidated.

2. Experimental

2.1. Sample preparation

Ingots of Mg−1Sn-xIn (x = 0, 0.5, 1, 1.5, 2 and 2.5 wt%) alloy were designed with commercial pure magnesium (Mg ≥ 99.99%) and pure tin (Sn ≥ 99.8%) and pure indium (In ≥ 99.99%), and were smelted in a PDM-1 type-inclined Mg-alloy furnace protected by a mixed gas (CO_2 + 0.2% SF_6). The melting temperature was maintained at 720 °C, the contents were stirred, and the slag was removed promptly. When the temperature of the melt was cooled to about 550 °C, the melt was poured into a right-angled stainless-steel mold to obtain an as-cast Mg ingot. Strict control of each step of the smelting process ensured that the smelting time and melt temperature as well as the melt environment were as consistent as possible to eliminate interference from other factors. The actual component of the investigated alloys was determined by inductively coupled plasma-atomic emission spectroscopy (ICP-AES) and the results are listed in Table 1. All alloy samples investigated were taken from the same surface and position.

2.2. Microstructural characterization

X-ray diffraction (XRD) revealing information about the chemical composition were conducted on a TD-3500 X-ray diffractometer using Cu K_α radiation at a scan speed of 2°/min and scan angles from 20° to 80°. The XRD spectra were analyzed using the MDI Jade 6.0 software. A scanning electron microscopy (SEM, TESCANVEGA3) was employed for the characterization of the microstructure and changes in the surface morphologies of alloy samples. The chemical composition and the element distribution maps of the alloys were obtained by the analysis of the micro-region composition with the energy dispersive spectroscopy (EDS, Oxford). The precipitate structures were analyzed using a JEM-F200 transmission electron microscopy (TEM), selected area electron diffraction (SAED) and high resolution electronic microscopy (HRTEM). Specimens for TEM were prepared by electropolishing a twin-jet electron polishing system in 3% $HClO_4$ and 97% ethanol at −35 °C. The surface morphologies of the investigated alloys were observed using a Prmotech-Mat type of metallographic microscope made by Carl Zeiss. Prior to starting the metallographic observation, all specimens were abraded with silicon carbide papers up to 2000-grit and then polished elaborately with diamond abrasive paste to a final polishing particle roughness of 0.5 μm, and 4% nitric acid alcohol was used to corrode. The chemical composition of the corrosion products were detected using X-ray photoelectron spectroscopy (XPS, ESCALAB 250). All binding energy values in the XPS spectrum were corrected using an indeterminate C_{1s} signal (set at 284.6 eV). The data was analyzed using the XPSPEAK 4.1 software.

Table 1
Composition of samples (in wt. %) determined by ICP-AES.

Alloys	Sn	In	Mg
Mg−1Sn	1.07	–	Bal.
Mg−1Sn-0.5In	1.21	0.46	Bal.
Mg−1Sn−1In	0.94	1.22	Bal.
Mg−1Sn-1.5In	1.13	1.71	Bal.
Mg−1Sn−2In	0.97	2.08	Bal.
Mg−1Sn-2.5In	1.15	2.69	Bal.

2.3. Electrochemical test

Polarization curves were obtained and electrochemical impedance spectroscopy (EIS) of Mg−Sn−In alloys carried out at an electrochemical workstation (SP-150; Bio-logic Science Instruments, Seyssinet-Pariset, France) equipped with a standard three-electrode cell. Specimens (a surface area of 1 cm^2 was exposed) were used as working electrodes, platinum mesh as the counter electrode, and a saturated calomel electrode (SCE) as the reference electrode. All potentials in this article are referred to as SCE unless indicated otherwise. A corrosive medium (3.5% NaCl solution at pH 6.8−7.3) for electrochemical testing was formulated with reagent-grade NaCl and deionized water. The temperature of the electrolyte controlled by the water bath of the thermostat was at 25 °C during the experiment.

All sample coupons were wet-abraded to 2000 grit and cleaned ultrasonically with anhydrous ethanol before each electrochemical test. Polarization curves were obtained and EIS undertaken after the sample coupons had been exposed to the corrosive medium for 15 min to ensure a stable system. The polarization curves were swept at a scan rate of 1 mV/s with a scan range of −200 mV/E_{corr} to +500 mV/E_{corr}. The Tafel extrapolation method was employed to fit the polarization curves. EIS measurements were carried out with an applied perturbation voltage of 5 mV over a frequency range from 100 kHz to 10 mHz. EIS spectra were fitted using ZSimpWin 3.30 software.

2.4. Immersion experiments

Measurement of mass loss was carried out and immersion experiments were done after exposure to 3.5 wt% NaCl solution at room temperature for various times. These parameters were estimated periodically to characterize the effect of the investigated alloys on the initiation and propagation of corrosion. To prevent the pH of the solution being affected by corrosion, the ratio of the sample area (in cm) to the volume of the prepared NaCl solution (in mL) was 1:300. At the end of the corrosion test, samples were rinsed with deionized water and dried in air immediately. To investigate the morphologies of the underlying (corroded) substrate of Mg-alloy samples, after surface characterization of the corrosion products, the investigated alloys were immersed in chromic acid (200 g/L of CrO_3 + 10 g/L of $AgNO_3$) aqueous solution for more than 5 min to dissolve the corrosion layer. Samples immersed for 5 days were used for mass-loss measurements and

weighed with a digital analytical balance with an accuracy of 0.0001 g. All experiments were done in triplicate to guarantee good reproducibility of the data.

3. Results

3.1. Microstructural analyses

The microstructures of as-cast Mg−Sn−In alloys, as depicted in Fig. 1, exhibited different dendritic microsegregation with changes in the In concentration. Smelting was carried out several times to eliminate other factors so that the microstructure was the true one. This was the result of following the preferred crystallographic directions in the solidification of the alloys, and the mean thickness of dendrite arms was approximately 20 μm. Due to the large difference in temperature at the mold−metal interface, the as-cast alloy formed an equiaxed region comprising many small crystals oriented randomly which grew rapidly into branches along their preferred crystallographic directions. Since the crystals in which the preferred orientation is antiparallel to the direction of the heat flow grow faster, the solid-liquid interface morphology is governed. The characteristics of the solidification structure are dependent upon the cooling conditions and alloy composition [38]. In the present study, the solidification environment of the alloy was controlled very carefully to study the effect of the amount of In on the morphologies of the formed alloys. However, the ratio of flow diffusion of In and Sn in the Mg melt was not consistent, and it was also related to the latent heat released continuously during solidification, so the morphology of dendrite segregation along the grain boundary differed. In and Sn were enriched at the grain boundaries, thereby causing segregation of the elements. The mechanism of such segregation is outside the scope of our study. The microstructures of the Mg−1Sn alloy (Fig. 1a) and Mg−1Sn-1.5In alloy (Fig. 1d) were characterized by typical dendritic morphology with a particular orientation. In the metallographic photograph of the Mg−1Sn alloy, the dark-gray areas on dendrites are where the Mg_2Sn phases are located, whereas the other regions are the Sn-containing solid solutions of α-Mg substrates, as denoted by the EDS results (Fig. 2a). For the sake of description, the dendritic region with a higher concentration of Sn was designated as the Tin-rich zone. Although it was not obvious under a metallographic microscope, the distribution of the Tin-rich zone and Mg_2Sn phases could be seen clearly using SEM. The excessive number of solute atoms in the Tin-rich zone precipitated in the form of the second phase (i.e., the Tin-rich zone was where Mg_2Sn phases were formed), which was attributed to the low solubility of Sn in α-Mg. For alloys containing In, the second phase (which was identified from the SAED pattern), remained in the Mg_2Sn phase (Fig. 3a). In Mg−Sn−In alloys, various microstructures were observed with a gradual increase in the In concentration from 0 wt% to 2.5 wt%. Upon solidification of the alloys, the In concentration at the dendrites increased gradually, and the mean concentration of In in the dendrites is summarized in Table 2. For Mg−1Sn-xIn (x = 0.5 and 1 wt%) alloys (Fig. 1b, c), a similar “dot”-like or “strip”-like morphology and a small amount of “flower”-like morphology was noted. This was attributed to the prominence of the Mg_2Sn phase relative to the lower In concentration of dendritic segregation elements. The continuity of the dendrites increased as the concentration of In increased, resulting in a strong strip-like morphology and flower-like morphology, such as those seen in Mg−1Sn-xIn (x = 1.5, 2 and 2.5 wt%) alloys (Fig. 1d−f). The continuity of the dendrite arms became clearer as the In concentration increased. Fig. 2b−f shows the SEM images of Mg−1Sn−1In alloy and the corresponding elemental distribution maps. Aggregation and non-uniformity of elements in the Mg−1Sn−1In alloy were revealed clearly in the elemental distribution maps. By scanning the surface of the Mg−1Sn−1In alloy, the In concentration in the dendrites was higher than that of the α-Mg matrix (Fig. 2f) (i.e., the Tin-rich zone was also the Indium-rich zone). TEM revealed that this area comprised many segregation phases (Fig. 3b). High-resolution TEM confirmed that this region contained two phases: Mg_3In (Fig. 3c) and Mg_2Sn (Fig. 3d). The presence of some Mg_3In phase and Mg_2Sn phase was why the concentrations of Sn and In in this region were higher than those in the matrix. For convenience, this area was designated the “Segregative phases zone”. The flower-like morphology of the Mg−1Sn−2In alloy could be expected because this morphology could prevent the propagation of corrosion.

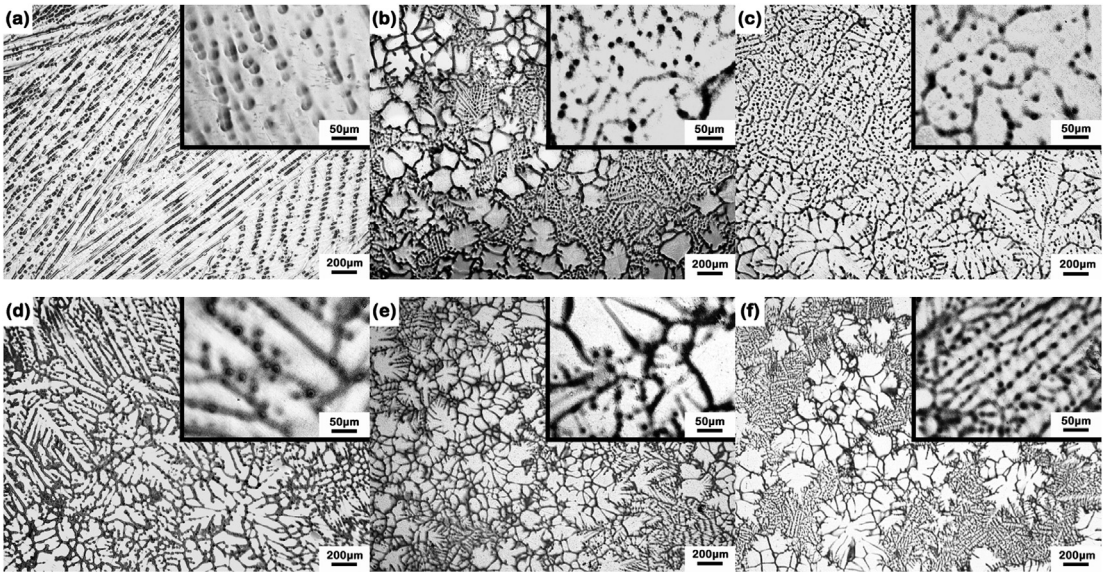

Fig. 1. The optical micrographs of as-cast alloys:(a) Mg−1Sn,(b) Mg−1Sn-0.5In, (c) Mg−1Sn−1In, (d) Mg−1Sn-1.5In, (e) Mg−1Sn−2In and (f) Mg−1Sn-2.5In.

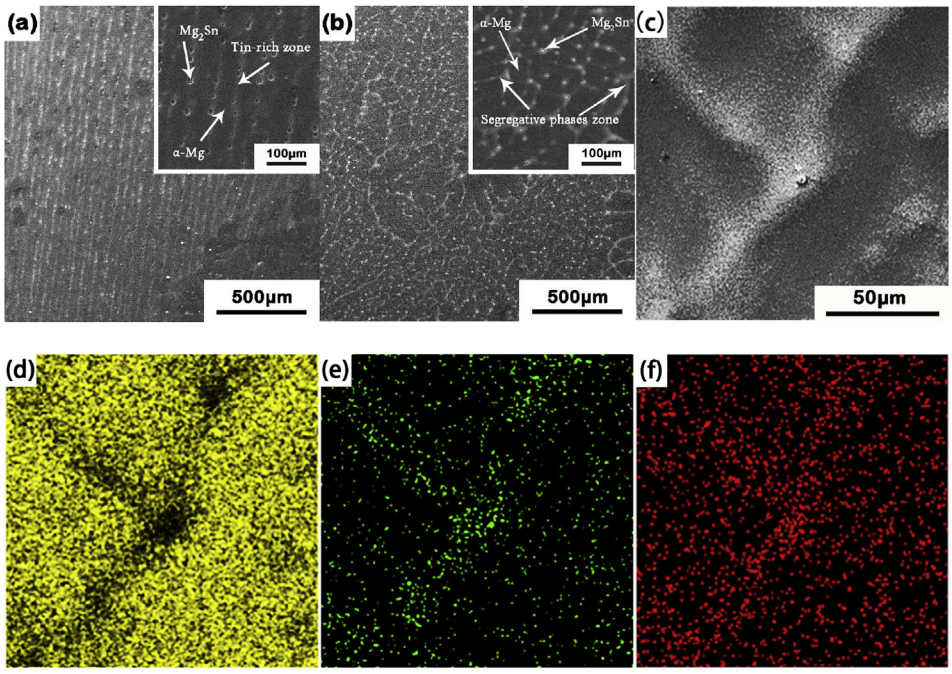

Fig. 2. SE images of Mg−1Sn(a), Mg−1Sn−1In alloy (b and c), and the corresponding elemental distribution maps of Mg (d), Sn (e), and In (f).

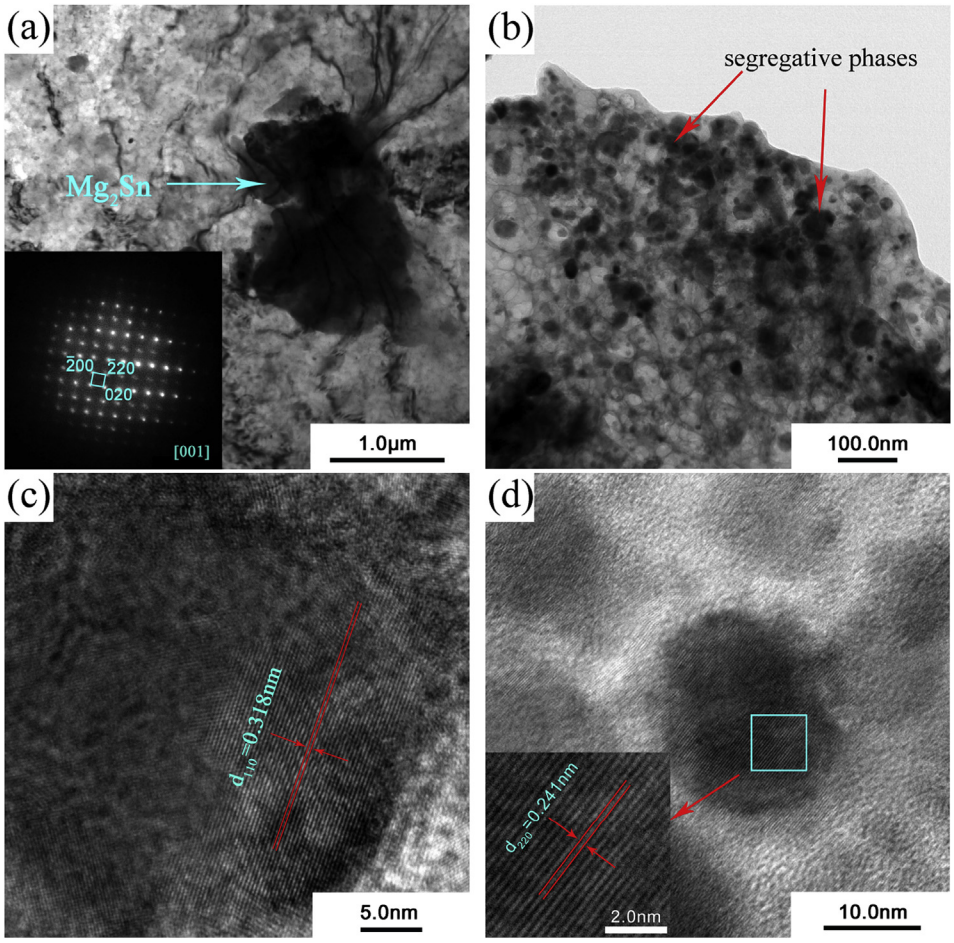

Fig. 3. TEM image of a typical precipitated phases or region of Mg−1Sn−2In alloy. (a) A larger size precipitate and its SAED. (b) Segregative phases zone. (c) and (d) HRTEM image of different precipitation phases.

Table 2
Concentrations (In wt.%) of the In elements in dendrites of the as-cast alloys (EDS).

	As-cast alloys					
	Mg−1Sn	Mg−1Sn-0.5In	Mg−1Sn−1In	Mg−1Sn-1.5In	Mg−1Sn−2In	Mg−1Sn-2.5In
dendrites	0	0.89	1.73	2.17	2.94	3.82

3.2. Mass-loss test

The corrosion rate of alloys can be studied intuitively from the mass-loss test. Fig. 4 is a histogram of the rate of mass loss due to corrosion of Mg−Sn−In alloys immersed in 3.5 wt% NaCl solution for 5 days. Measuring the pH (7.9−8.3) of the immersion for 5 days revealed that the pH increased slightly, which was attributed to formation of the alkaline $Mg(OH)_2$. Although the pH increased slightly, the impact on the analysis in our study was negligible. The mass-loss experiment demonstrated that the corrosion resistance of the six alloys increased in the order Mg−1Sn−1In < Mg−1Sn-0.5In < Mg−1Sn < Mg−1Sn-1.5In < Mg−1Sn-2.5In < Mg−1Sn−2In. Calculation of the rate of mass loss due to corrosion revealed that the Mg−1Sn−2In alloy exhibited the lowest corrosion rate (6.692 mm/y), which reflected the optimum corrosion resistance. The highest corrosion rate was observed for the Mg−1Sn−1In alloy (11.018 mm/y), which reflected the worst corrosion resistance. The histogram shows that the corrosion rate of the alloys increased initially and then decreased as the In concentration increased.

3.3. Polarization behaviors

Fig. 5 shows the polarization curves of Mg−Sn−In alloys in 3.5 wt% NaCl solution. After the polarization test, the pH (7.1−7.5) of the solution barely affected the data. The polarization curves of the Mg−1Sn-xIn (x = 0, 0.5 and 1 wt%) alloys (Fig. 5a) revealed that the corrosion potential of the Mg−1Sn alloy was the most negative, whereas the most positive corrosion potential was for the Mg−1Sn−1In alloy. Addition of In (0−1 wt.%) made the corrosion potential of the alloys more positive, but also increased the corrosion current density of the studied alloys. An apparent breakdown potential was present on each anodic side of the Mg−1Sn-xIn (x = 0, 0.5 and 1 wt%) alloys (which are marked on the curves), which showed the presence of oxide films. The polarization curves of the Mg−1Sn-xIn (x = 1.5, 2 and 2.5 wt%) alloys (Fig. 5b) were controlled mainly by the anode reaction. There were two breakdown potentials on each anode side of the Mg−1Sn-xIn (x = 1.5, 2 and 2.5 wt%) alloys, indicating that they possessed a denser double corrosion layer or an incomplete stacked multilayer film.

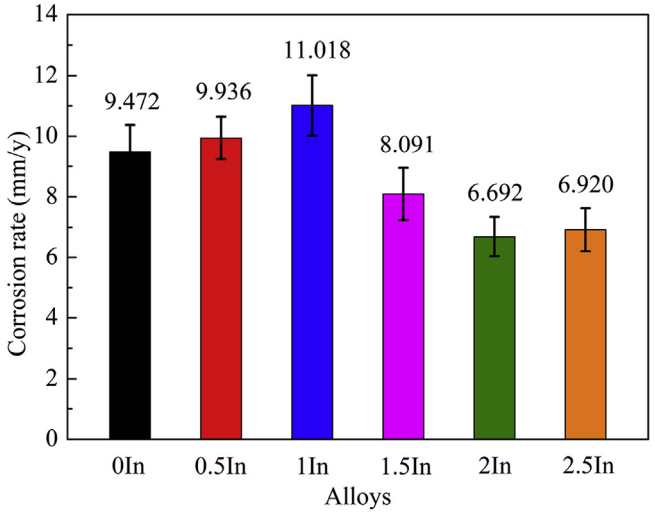

Fig. 4. Mass loss method for measuring corrosion rate of Mg−Sn−In alloys in 3.5 wt% NaCl solution.

The polarization curves were fitted using EC-Lab™ software (Bio-Logic Instruments) in the Tafel (conventional) model (Table 3). The i_{corr} can reflect the corrosion resistance of an alloy. For Mg−Sn−In alloys, the i_{corr} increased in the order Mg−1Sn−2In < Mg−1Sn-2.5 < Mg−1Sn-1.5In < Mg−1Sn < Mg−1Sn-0.5In < Mg−1Sn−1In. The Mg−1Sn−2In alloy exhibited the lowest corrosion current density (4.566 μA). The corrosion current density of Mg−1Sn-xIn (x = 1.5, 2 and 2.5 wt%) alloys was lower than that of Mg−1Sn-xIn (x = 0, 0.5 and 1 wt%) alloys, illustrating that a certain amount of In can reduce the corrosion current density of the alloy.

3.4. EIS

Interfacial processes and corrosion mechanisms are investigated by electrochemical impedance spectroscopy (EIS) to obtain the electrode interface structure and kinetic information of the alloy during the corrosion process [39]. The EIS spectra of the Mg−Sn−In alloys immersed for 15 min are shown in Fig. 6. Interfacial processes and corrosion mechanisms can be investigated by EIS to demonstrate the structure of the electrode interface and kinetic information of the alloy during corrosion [39]. The EIS data of the Mg−Sn−In alloys after immersion for 15 min are shown in Fig. 6. After EIS measurement, the pH (6.9−7.3) of the solution remained essentially unchanged, barely affecting the measurement data. The Nyquist plots of the six alloys were similar (Fig. 6a), comprising three loops: one capacitive loop at high frequency, one capacitive loop at medium frequency, and one inductive loop at low frequency. The capacitive loops at high frequency were related to electron transfer and the electrochemical double-layer. The larger the loop radius, the larger was the charge-transfer resistance, and the harder was the corrosion. The radius of the loops at high frequency increased according to the order Mg−1Sn−1In < Mg−1Sn-0.5In < Mg−1Sn < Mg−1Sn-1.5In < Mg−1Sn-2.5In < Mg−1Sn−2In. Hence, the radius of the loop of the Mg−1Sn−2In alloy was the largest, and the radius of the loop of the Mg−1Sn−1In alloy was the smallest. The capacitive loop at medium frequency was related to formation of a corrosion layer. Inductive loops were present in all six alloys at low frequency, which could be attributed to the interaction of corrosion products during partial dissolution of the localized corrosion layers [20,40]. Bode plots of |Z| *vs.* frequency are shown in Fig. 6b. The impedance from the high-frequency area to the mid-frequency area increased gradually, and the impedance in the low-frequency area decreased. The Mg−1Sn−2In alloy possessed the highest impedance, whereas the Mg−1Sn−1In alloy exhibited the lowest impedance. Bode plots of degree *vs.* frequency showed the existence of three time constants corresponding to the capacitive loops at high and medium frequency and the inductive loop at low frequency observed in Fig. 6c. Therefore, the EIS results showed that the corrosion resistance of the six alloys increased in the order Mg−1Sn−1In < Mg−1Sn-0.5In < Mg−1Sn < Mg−1Sn-1.5In < Mg−1Sn-2.5In < Mg−1Sn−2In. The Mg−1Sn−2In alloy exhibited the optimal corrosion resistance, whereas the Mg−1Sn−1In alloy showed the worst corrosion resistance.

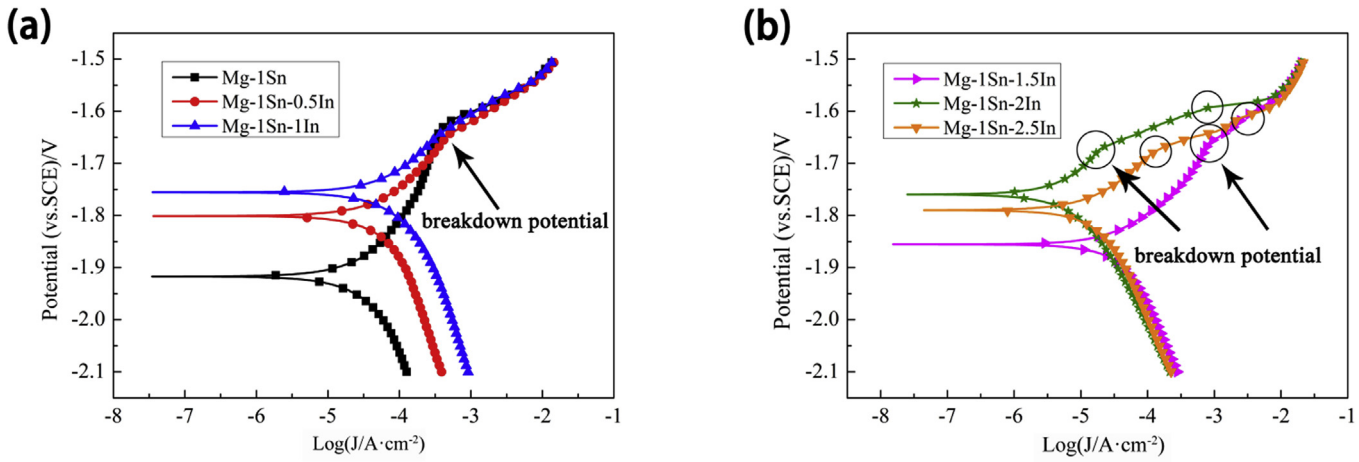

Fig. 5. Polarization curves of the Mg−Sn−In alloys in 3.5 wt% NaCl solution: (a) Mg−1Sn-xIn (x = 0, 0.5 and 1 wt%) alloys; (b) Mg−1Sn-xIn (x = 1.5, 2 and 2.5 wt%) alloys.

Table 3
Fitting results from potentiodynamic polarization curves.

Mg alloys	E_{corr} (vs.SCE)/V	i_{corr} (μA cm^{-2})	b_a(mV/decade)	$-b_c$ (mV/decade)
Mg−1Sn	−1.917	32.6	224.1	305.7
Mg−1Sn-0.5In	−1.801	53.2	160.6	291.4
Mg−1Sn−1In	−1 .755	55.1	136.1	177.8
Mg−1Sn-1.5In	−1.855	28.1	105.5	195.7
Mg−1Sn−2In	−1 .759	4.6	139.2	136.6
Mg−1Sn-2.5In	−1.790	12.5	113.8	186.9

More specifically, to gain clearer insights into the corrosion characteristics of the Mg−Sn−In alloys, the impedance response was modeled using an equivalent electrical circuit (EEC) (Fig. 7). The main EIS parameters for fitting the EEC using ZSimpWin 3.30 are listed in Table 4. A constant-phase element was used to model the non-ideal capacitive behavior of the electrode [39]. The EEC fitting parameters for the investigated alloys could be interpreted: Q_1 and R_{ct} described the constant-phase component for the electrochemical double-layer and charge transfer resistance, respectively; Q_2 and R_f described the capacitance and resistance of the $Mg(OH)_2$ film, respectively; R_L and L described the inductance resistance and inductance at low frequency due to the partial breakdown of the $Mg(OH)_2$ protective film, respectively; R_s described the solution resistance. R_{ct}, to some extent, determines the corrosion resistance of the material; the larger the R_{ct}, the better is the corrosion resistance. The R_{ct} of the Mg−1Sn−2In alloy reached 771.4 Ω, whereas the R_{ct} of the Mg−1Sn−1In alloy was 448.7 Ω. R_f reflected the compactness and thickness of the film and other conditions; the larger the R_f, the greater was the corrosion resistance of the film, and the better was the protection of the film. For the Mg−1Sn−2In alloy, a significantly larger R_f (286.0 Ω) with respect to that of the Mg−Sn−In alloys was observed, which revealed the best protection of its corrosion layer, whereas the R_f of the Mg−1Sn−1In alloy was 29.3 Ω, with poor protection of the corrosion layer. R_{ct} and R_f first decreased and then increased as the In concentration increased (Table 4), so the corrosion resistance of the alloys had the same pattern of change.

3.5. Observation of corrosion morphology

The corrosion morphologies of the Mg−Sn−In alloys immersed in 3.5 wt% NaCl solution for 5 h are shown in Fig. 8. The corrosion morphology was dependent primarily on the microstructure of the alloy. According to the association between microstructure and corrosion morphology, the latter can be classified as corrosion types of “dot-based”, “strip-based” or “sheet-like”. The corrosion morphology of the Mg−1Sn alloy was similar to that of the Mg−1Sn-1.5In alloy, which was mainly strip-shaped. The corrosion products of the Mg−1Sn alloy (Fig. 8a) and Mg−1Sn-1.5 alloy (Fig. 8d) had a particular orientation, which was in accordance with the metallographic photograph in Fig. 1. Simultaneously, regular pitting corrosion products were observed clearly in the corrosion morphology of the Mg−1Sn alloy, indicating that corrosion started around the Mg_2Sn phases and then formed strip-like corrosion areas. The corrosion morphology of the Mg−1Sn-0.5In alloy (Fig. 8b) and Mg−1Sn−1In alloy (Fig. 8c) was similar, showing a continuous layer of corrosion products on the surface of the alloy. Formation of “flaky” corrosion products revealed that the initiation and propagation of corrosion was very fast, and was related to the morphology of the microstructure. That is, the dot-like microstructures of the Mg−1Sn-0.5In alloy and Mg−1Sn−1In alloy could initiate corrosion rapidly and did not prevent corrosion propagation. There was also a similar relationship between the corrosion patterns of the Mg−1Sn−2In alloy (Fig. 8e) and Mg−1Sn-2.5In alloy (Fig. 8f). Corrosion products were present in individual, small pieces and were not bonded into sheets. This was attributed mainly to the microstructures of the strip-like morphologies and flower-like morphologies. The microstructures of the strip-like morphologies and flower-like morphologies of the Mg−1Sn−2In alloy were more uniform than those of the Mg−1Sn-2.5In alloy. The amount of the corrosion products increased in the order Mg−1Sn−2In < Mg−1Sn-2.5In < Mg−1Sn-1.5In < Mg−1Sn < Mg−1Sn-0.5In < Mg−1Sn−1In. Hence, the Mg−1Sn−2In alloy showed the best corrosion resistance, and the Mg−1Sn−1In alloy exhibited the most serious corrosion.

The Mg−1Sn−1In alloy was selected as the research object of the corrosion process. The corrosion morphologies of the Mg−1Sn−1In alloy immersed in 3.5 wt% NaCl solution for 1, 3 and 5 h are shown in Fig. 9. Fig. 9a shows the distribution of corrosion

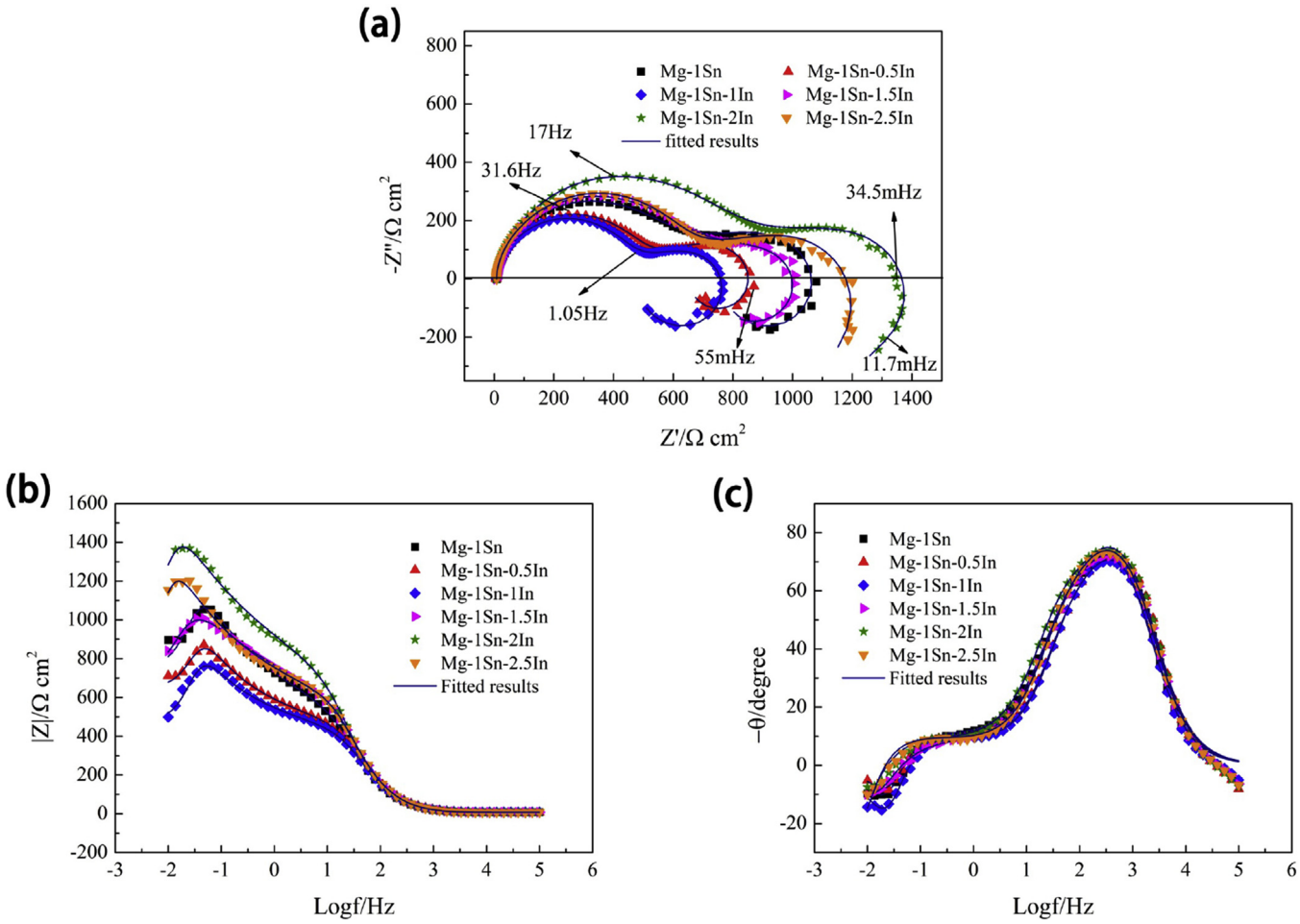

Fig. 6. EIS spectra of the Mg−Sn−In alloys in 3.5 wt% NaCl solution: (a) Nyquist plots; (b) and (c) Bode plots.

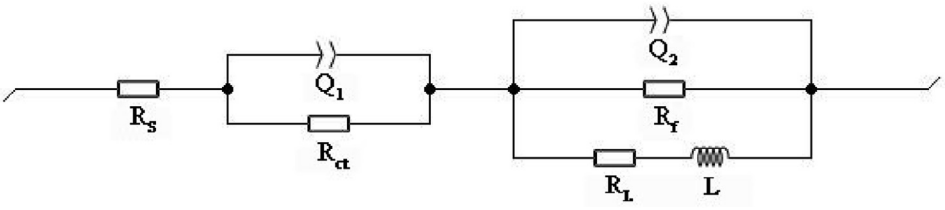

Fig. 7. Equivalent electrical circuit of the EIS spectra.

Table 4
Electrochemical parameters of Mg−Sn−In alloys obtained by fitting the electrochemical impedance spectra in Fig. 6.

Specimens	R_s (Ω cm^2)	Q_1 (F/cm 2)	Freq,n	R_{ct}(Ω cm^2)	Q_2 (F/cm 2)	Freq,n	R_f(Ω cm^2)	R_L(Ω cm^2)	L (H/cm^2)	Chi-squared
Mg−1Sn	7.604	1.621E-05	0.9390	574.8	1.151E-03	0.7714	135.3	362	3093	0.003864
Mg−1Sn-0.5In	7.047	1.217E-05	0.9597	474.1	1.54E-03	0.7628	43.69	344.8	4172	0.004853
Mg−1Sn−1In	8.321	1.303E-05	0.9577	448.7	2.024E-03	0.7541	29.3	300.2	1833	0.002763
Mg−1Sn-1.5In	7.803	1.311E-05	0.9505	612.3	1.121E-03	0.7847	66.01	318.2	4595	0.003527
Mg−1Sn−2In	6.746	1.417E-05	0.9483	771.4	1.334E-03	0.7819	286	425.5	5130	0.00552
Mg−1Sn-2.5In	7.448	1.28E-05	0.9556	644	1365E-03	0.729	126	395.2	4890	0.003815

products along the Segregative phases zone. The high-magnification image shows that the corrosion products accumulated around the Mg_2Sn phases and formed a strip of corrosion traces along the Segregative phases zone. Fig. 9b reveals the corrosion morphology of the surface covered with a thin layer of corrosion products. The high-magnification image demonstrates the Segregative phases zone to be covered by corrosion products, whereas the black-gray matrix had no coverage after initial immersion in 3.5% wt.% NaCl solution for 3 h. Obviously, most of the areas are corroded in Fig. 9c; high magnification shows that the

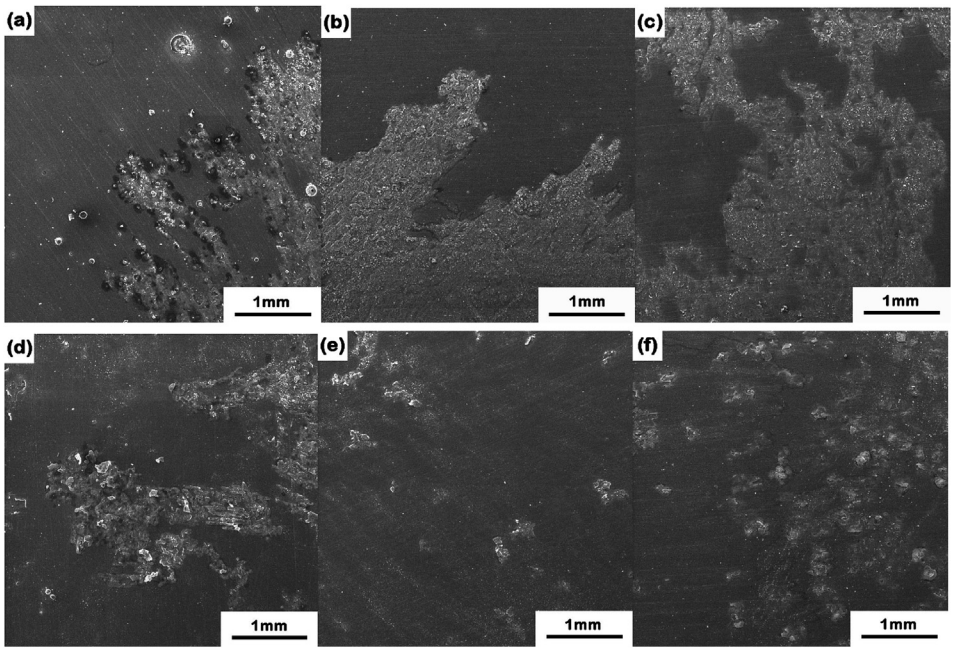

Fig. 8. The corrosion morphologies of the Mg−Sn−In alloys immersed in a 3.5 wt% NaCl solution for 5 h: (a) Mg−1Sn,(b) Mg−1Sn-0.5In, (c) Mg−1Sn−1In, (d) Mg−1Sn-1.5In, (e) Mg−1Sn−2In and (f) Mg−1Sn-2.5In.

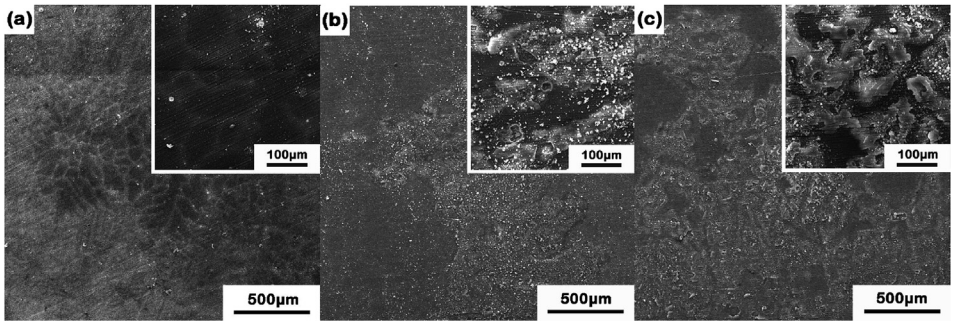

Fig. 9. Corrosion morphologies of Mg−1Sn−1In alloy after immersion in 3.5 wt% NaCl solution for (a) 1 h, (b) 3 h and (c) 5 h.

corrosion extended into the α-Mg matrix, forming loosely corroded sheets of corrosion products with low protection to the matrix.

The SEM image (Fig. 10a) of the de-corroded products of the Mg−1Sn alloy exhibited a row of neatly etched “gully”-like shapes consistent with the metallographic image, thereby confirming that the corrosion zone proceeded along the boundary between the Tin-rich zone and α-Mg matrix. Nevertheless, there were some obvious corrosion pits in the area where no gullies had been formed, which was caused mainly by the potential difference between the Mg_2Sn phases and ambient Tin-rich zone. The gullies formed by removing the corrosion products of the Mg−1Sn−1In alloy conformed to the metallographic structure, and the corrosion trace propagated in the form of dendrites (Fig. 10b). This type of corrosion was comprehensive and spread rapidly throughout the alloy surface. Fig. 10c is a magnified view of Fig. 10b, with corrosion characteristics and details presented clearly. Various positions of the alloy were measured by EDS, and the corresponding elemental concentrations are shown in the subsequent figures. The mark “1” is the α-Mg matrix, and the areas labeled “2”, “3” and “4” are the Segregative phases zone (Fig. 10c(1–4)). It is apparent from the boundary of corrosion and non-corrosion that corrosion occurred along the boundary between the Segregative phases zone and α-Mg matrix. It is reconfirmed that the α-Mg matrix was more susceptible to corrosion than the Segregative phases zone. Hence, the Segregative phases zone exhibited cathode characteristics relative to the α-Mg matrix. Certainly, since there were a large number of finely dispersed Mg_3In phases and Mg_2Sn phases in the segregative phases zone, the Segregative phase zone was also dissolved. Fig. 10d demonstrates that corrosion occurred only in certain dispersed regions of the Mg−1Sn−2In alloy. These dispersed areas were determined by the microstructure of the flower-like morphology, which hindered the propagation of corrosion.

Fig. 11a is an XRD image of the corrosion products. Comparison of the positions of the peaks revealed that all were the characteristic peaks of $Mg(OH)_2$. To confirm further the chemical composition of the corrosion products, XPS was used to detect low-concentration elements and their valence states in view of the fact that the measured elements Sn and In were at the limit of detection according to XRD. Fig. 11b and c are decomposition-fitted curves of XPS spectra of Sn3d and In3d, respectively. Fig. 11b reveals that the high-resolution spectrum of Sn3d contains two peaks. By peak-fitting and comparison with the standard binding energy, the peak of $Sn3d_{5/2}$ could be decomposed into a characteristic peak of Sn with a binding energy of 484.9 eV and a characteristic peak of

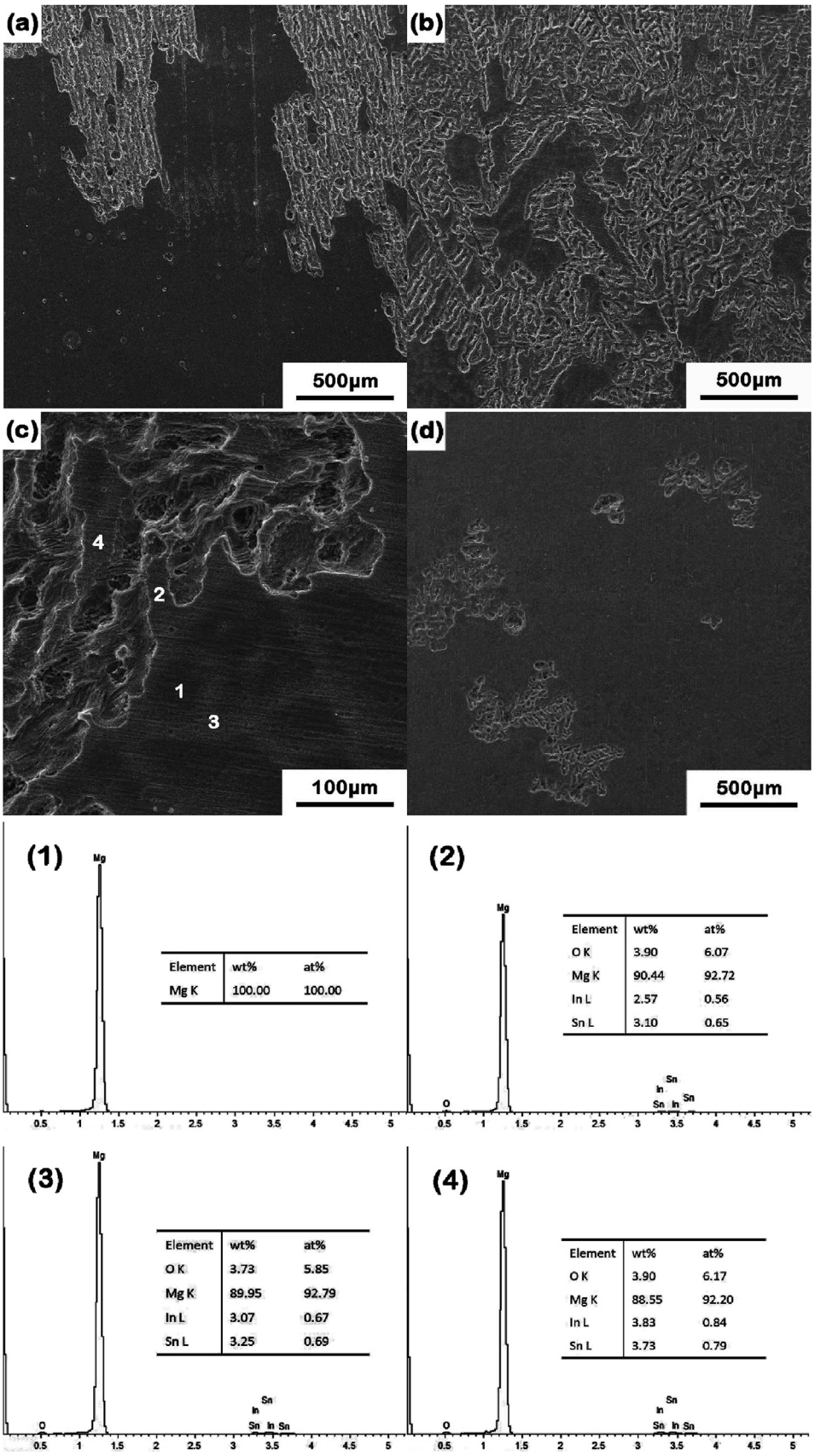

Fig. 10. Corrosion morphologies of de-corrosion products after immersion of (a) Mg−1Sn, (b) and (c) Mg−1Sn−1In, (d) Mg−1Sn−2In alloys in a 3.5 wt% NaCl solution for 5 h and the corresponding EDS element content, and (1), (2), (3) and (4) corresponds to each marked of Fig. 10c.

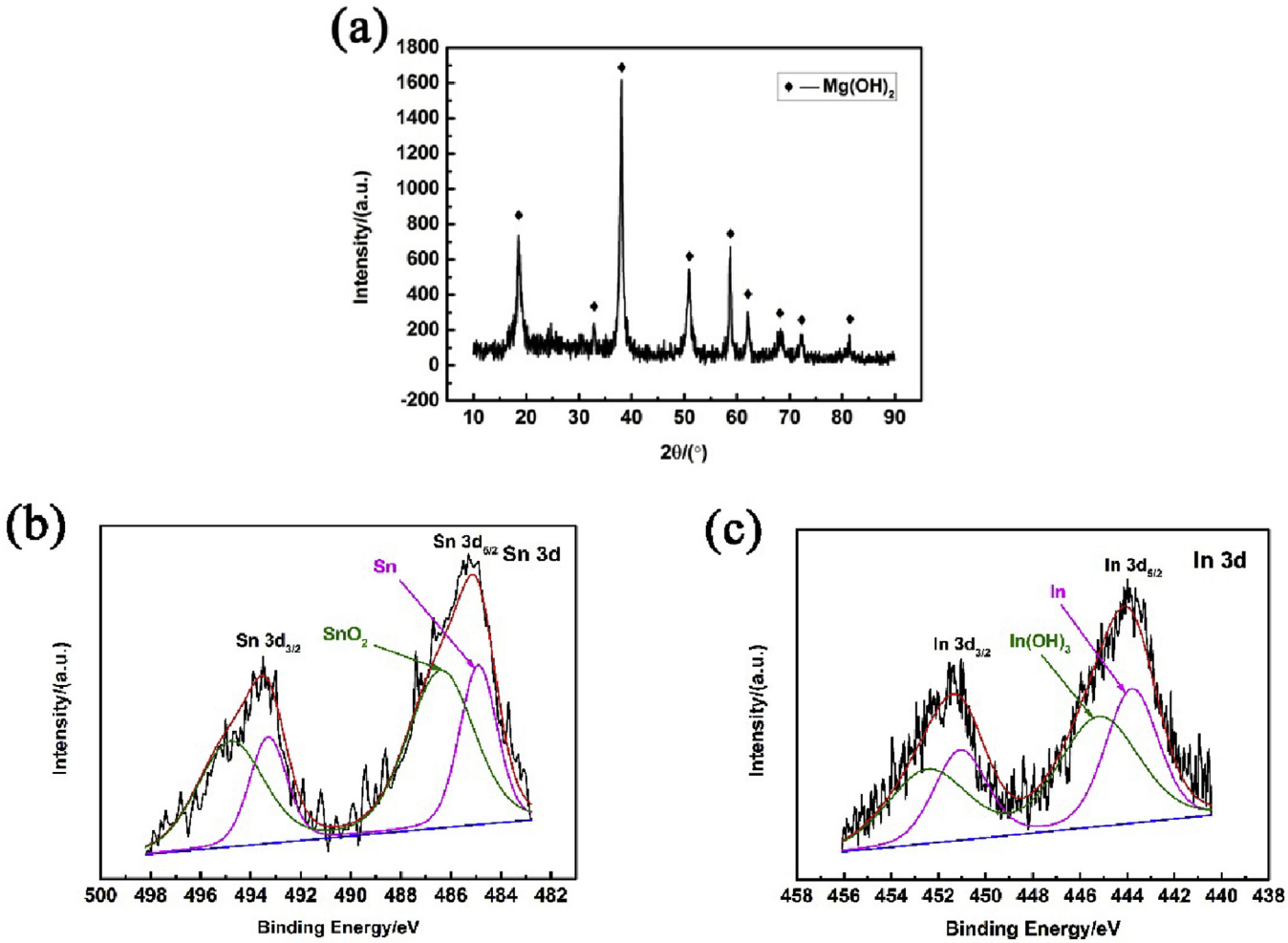

Fig. 11. Composition characteristics of corrosion products for Mg−1Sn−2In alloy: XRD patterns (a), XPS spectrum Sn3d (b), and In3d (c).

SnO_2 with binding energy of 486.4 eV. In the same way, the peak of $In3d_{5/2}$ in Fig. 11c could be decomposed into an In characteristic peak with binding energy of 443.8 eV and characteristic peak of $In(OH)_3$ with a binding energy of 445.1 eV. Surprisingly, the presence of In and Sn in the corrosion products confirmed that the dissolved In^{3+} and Sn^{4+} had undergone reduction. The existence of these substances would inevitably affect the characteristics of the films.

4. Discussion

4.1. Relationship between dendrite segregation and corrosion resistance

If the microsegregation of Mg−Sn alloys cannot be eliminated, the microsegregation must be adjusted to obtain a more corrosion-resistant microstructure. With regard to Mg−Sn−In alloys, the addition of In affects the orientation of dendritic segregation during solidification, and presents various morphologies. Corrosion of the Mg−1Sn alloy and Mg−1Sn-1.5In alloy proceeded with strip-like corrosion morphology along a certain orientation, and corrosion propagation could not be prevented. The corrosion morphologies and metallographic microstructures of the Mg−1Sn-0.5In alloy (Fig. 8b) and Mg−1Sn−1In alloy (Fig. 8c) were similar. The Mg_2Sn phases were conspicuous compared with the surrounding Segregative phases zone at lower concentrations, so the metallographic images showed analogously dot-like morphologies. When immersed in a corrosive medium, there was a comparatively large potential difference between Mg_2Sn phases and the peripheral Segregative phases zone. Furthermore, the lower concentration of the Segregative phases zone could not restrict corrosion propagation satisfactorily, and a continuous sheet-like layer of corrosion products was formed. Mg−1Sn-xIn (x = 2 and 2.5 wt%) alloys with many strip-like and flower-like morphologies had similar corrosion morphologies. When corrosion was initiated, the flower-like structure prevented the propagation of corrosion efficiently, resulting in formation of isolated corrosion areas. The Mg−1Sn−2In alloy possessed a more uniform distribution of strip-like and flower-like morphologies, and the isolation was stronger. Accordingly, the Mg−1Sn−2In alloy exhibited the best corrosion resistance, as we expected.

4.2. Effect of In concentration on the corrosion resistance of Mg−Sn−In alloys

Initially, the reprecipitation behavior of In was used to explain how In was activated in an Al sacrificial anode, as proposed by Reboul et al. [41], and this theory was accepted by many scholars

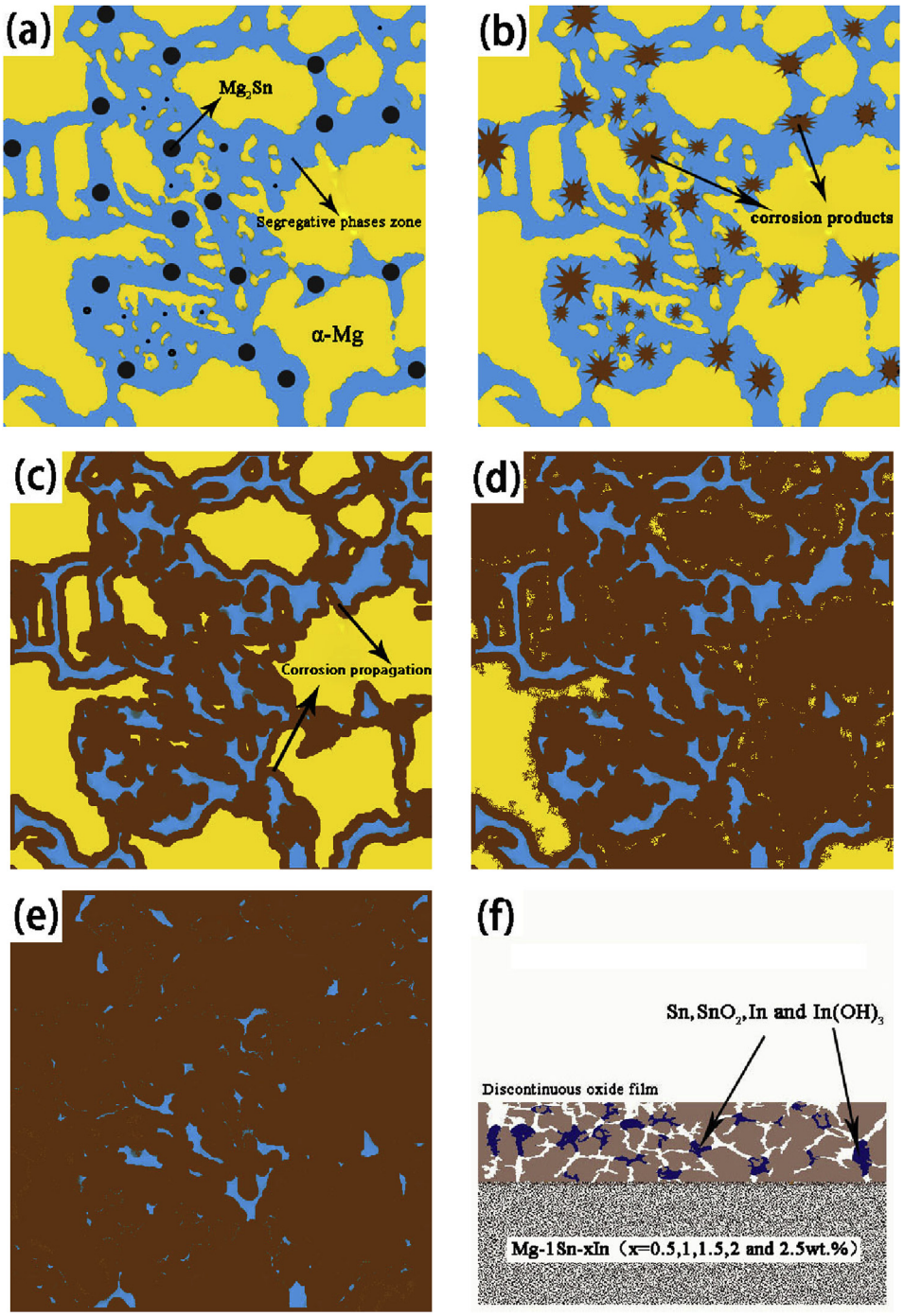

Fig. 12. (a-e) Schematic diagram of the corrosion process of the surface morphology of Mg−1Sn−2In alloy at different stages. (f) The cross-section mechanism diagram of the corrosion product containing In alloy.

[42−45]. Gore et al. [46] also observed In deposition on the Mg surface in a dilute solution of NaCl in the presence of In^{3+}. Li et al. [47] believed that this reprecipitation behavior could explain In-induced Mg activation, and that the equations for In activation were:

$$Mg\ (In) \rightarrow Mg^{2+} + In^{3+} + 5e^{-} \quad (1)$$

$$3\ Mg + 2In^{3+} \rightarrow 3Mg^{2+} + 2In \quad (2)$$

The In^{3+} produced by Equation (1) participates in Equation (2) to accelerate activation. The generated In atoms undergo the reaction of Equation (1), and this reaction cycle acts as activation [37].

The appearance of Sn suggests that similar reactions occurred. Ha et al. [48] considered that metallic Sn is enriched spontaneously on the surface of the Mg matrix. This action coincides with the presence of Sn or a Sn-accumulated layer observed by some researchers [25,49,50].

In this way, it is rational that In and Sn are present in the corrosion layers. Actually, corrosion activation/inhibition of the Mg alloys during the reaction process is quite ambiguous, but it can be

analyzed specifically according to the reaction process and formation conditions of alloys. That is, if the reaction process does not cause excessive disturbance at the corrosion layer and the reaction is in a relatively closed environment, a protective corrosion layer containing In and Sn can be formed.

The corrosion resistance of Mg alloys is closely related to the corrosion products formed on the surface, and protection of the films is dependent mainly on its compactness. In the present study, the existence of Sn, SnO_2, In and $In(OH)_3$ in the corrosion products of the Mg−Sn−In alloys filled the loose $Mg(OH)_2$ films to a certain extent, resulting in an increase in the compactness of $Mg(OH)_2$ films. Consequently, the protective characteristics of $Mg(OH)_2$ films were improved. However, activation of In and Sn also had a key role, which requires comprehensive consideration of the effect of the In concentration on Mg−Sn alloys.

If the concentration of In is low (0−1 wt.%), a non-densified corrosion layer containing a small amount of In oxide may be formed, and the activation effect of In is remarkable. At this time, no enclosed space can be formed, and the formation of In and Sn cannot accumulate effectively and play an active part. If the concentration of In increases (1−2 wt.%), a more compact corrosion layer can be formed. This is attributed to enhancement of In activation, and enhancement of the corrosion layer jointly controls the corrosion resistance of the alloy. More In and Sn accumulated on the film, which increased its compactness. Simultaneously, the increase in the insulation effect of the film was conducive to the formation of In and Sn. This mutually reinforcing cyclical process made the corrosion layer more dense and enhanced the corrosion resistance greatly. If the concentration of In continued to increase (2−2.5 wt%), the protective ability of the film formed under natural conditions was maximized. At this time, In no longer affected the compactness of the film. The corrosion rate tends to be related to other factors, such as microstructures. The results showed that In activation and the compactness of the corrosion layer affected the corrosion resistance of the material mutually, and the effect between the two was dependent upon which was more dominant. In addition, the corrosion products of Mg−1Sn-xIn (x = 0, 0.5 and 1 wt %) alloys exfoliated during immersion, and exfoliation of the corrosion products of the Mg−1Sn−1In alloy was greater than that of the Mg−1Sn-0.5In alloy. Significant exfoliation corrosion products were not observed in the Mg−1Sn-xIn (x = 1.5, 2 and 2.5 wt%) alloys, which also confirmed that the compactness of the film was very important.

4.3. Corrosion mechanism

The schematic diagram of the corrosion process on the surface morphologies of the Mg−1Sn−2In alloy at different stages and the cross-sectional mechanism diagram of corrosion products of Mg−Sn−In alloys are depicted in Fig. 12. The yellow regions represent α-Mg solid solutions containing In and Sn (generally considered to be the α-Mg matrix) and the blue striped regions represent the Segregative phases zone. Black dots represent Mg_2Sn phases, whereas brown regions represent corrosion products. For the longitudinal section, the upper light-brown areas represent a discontinuous corrosion layer and the blue areas represent a mixture of Sn, In, SnO_2 and $In(OH)_3$. The Mg_2Sn phases are at the intersection of the Segregative phases zone, and the edge of the Segregative phases zone is in contact with the α-Mg matrix (Fig. 12a). Experiments have confirmed that the Mg_2Sn phase exhibited cathodicity when in contact with the Segregative phases zone, and Segregative phases zone also exhibits cathodicity when in contact with the α-Mg matrix. Therefore, when the Mg−1Sn−2In alloy was immersed in 3.5 wt% NaCl solution, the corrosion originated from the periphery of the Mg_2Sn phases, resulting in initiation of corrosion (Fig. 12b). Thereafter, propagation was along the boundary between the Segregative phases zone and α-Mg matrix (Fig. 12c), and the potential difference between the two provided a driving force for erosion. As the immersion time of the Mg−1Sn alloy in 3.5 wt% NaCl solution increased, the α-Mg matrix corroded gradually, leaving the Segregative phases zone (Fig. 12d). Finally, the Segregative phases zone was corroded and the final corrosion of the surface was completed (Fig. 12e). In the corrosion process, the amount of the mixture of Sn, In, SnO_2 and $In(OH)_3$ varied with the alteration in In activation caused by the In concentration. Therefore, the degree of void-filling in the loose $Mg(OH)_2$ film was different, and resulted in the different compactness of the corrosion layer (Fig. 12f). The corrosion resistance of the alloy was controlled by In activation and the compactness of the corrosion layer. To prevent the discrepancy of corrosion resistance caused by a solid solution of In, the effect of In dissolved in the α-Mg matrix on the corrosion resistance of the alloys was investigated specifically. If the In concentration was >0.5 wt%, the In concentration barely affected the corrosion resistance of the alloy. The relevant main experimental results are listed in Table 5, and the obtained experimental results are not described in detailed.

5. Conclusions

1. The addition of In modified elemental segregation and resulted in different morphologies. Among them, the flower-like morphology of Mg−1Sn−2In was most effective in preventing the propagation of corrosion.
2. The corrosion resistance of Mg−1Sn-xIn (x = 0, 0.5, 1, 1.5, 2 and 2.5 wt%) alloys first decreased and then increased as the In concentration increased. This was influenced mainly by a combination of the microstructure of the alloys, In activation, and the compactness of the corrosion layer.
3. The corrosion resistance of the obtained Mg−1Sn−2In alloy was optimal according to a hypothesis test. The minimum corrosion rate of the Mg−1Sn−2In alloy was 6.692 mm/y, the i_{corr} was 4.566 μA, R_{ct} was 771.4 Ω, and R_f was 286.0 Ω.
4. Formation of a layer of corrosion products led to interaction between In activation and the compactness of the corrosion layer. When the In concentration was 2%, the interaction between the In activation of the alloy and compactness of the corrosion layer was optimal.
5. The corrosion process of Mg−1Sn-xIn (x = 0.5, 1, 1.5, 2 and 2.5 wt %) alloys was discovered. Primarily, corrosion was initiated at the periphery of the Mg_2Sn phases. Then, propagation was carried out along the boundary between the Segregative phases zone and α-Mg matrix. Thereafter, the α-Mg matrix corroded gradually and, eventually, the Segregative phases zone dissolved gradually.

Table 5
Corrosion rate and corrosion current density results of Mg−In binary alloys.

Mg-xIn alloys	x = 0.05	x = 0.1	x = 0.2	x = 0.3	x = 0.5	x = 1	x = 2
Corrosion rate(mm/y)	11.8	11.36	10.53	9.44	6.87	6.82	6.85
i_{corr} (μA cm^{-2})	40.82	36.11	23.27	21.33	10.71	7.93	8.35

Acknowledgements

This work was supported by the Key Scientific Research Project in Shanxi Province (Grant No. MC2016-06, 201603D111004, 20181101014 and 201805D121003), Research Project Supported by Shanxi Scholarship Council of China (2017-029), Patent Promotion and Implement Found of Shanxi Province (20171003), Corrosion and Protection Engineering Technology Research Center of Shanxi Province

References

[1] N.D. Nam, M. Mathesh, M. Forsyth, D.S. Jo, Effect of manganese additions on the corrosion behavior of an extruded Mg-5Al based alloy, J. Alloy. Comp. 542 (2012) 199–206.
[2] M.J. Nayyeri, F. Khomamizadeh, Effect of RE elements on the microstructural evolution of as cast and SIMA processed Mg-4Al alloy, J. Alloy. Comp. 509 (2011) 1567–1572.
[3] Z. Yin, Y. Chen, H. Yan, G.H. Zhou, X.Q. Wu, Z. Hu, Effects of the second phases on corrosion resistance of AZ91-xGd alloys treated with ultrasonic vibration, J. Alloy. Comp. 783 (2019) 877–885.
[4] B.J. Hopkins, S.H. Yang, D.P. Hart, Suppressing corrosion in primary aluminum-air batteries via oil displacement, Science 362 (2018) 658–661.
[5] G.L. Song, A. Atrens, Corrosion mechanisms of magnesium alloys, Adv. Eng. Mater. 1 (1999) 11–33.
[6] J.H. Nordlien, S. Ono, N. Masuko, K. Nisancioglu, A TEM investigation of naturally formed oxide films on pure magnesium, Corros. Sci. 39 (1997) 1397–1414.
[7] J.C. Fuggle, L.M. Watson, D.J. Fabian, S. Affrossman, X-ray photoelectron studies of the reaction of clean metals (Mg, Al, Cr, Mn) with oxygen and water vapour, Surf. Sci. 49 (1975) 61–76.
[8] X. Zhang, Y. Wu, Y. Xue, Z. Wang, L. Yang, Biocorrosion behavior and cytotoxicity of a Mg-Gd-Zn-Zr alloy with long period stacking ordered structure, Mater. Lett. 86 (2012) 42–45.
[9] Y. Song, D. Shan, R. Chen, E.H. Han, Effect of second phases on the corrosion behaviour of wrought Mg-Zn-Y-Zr alloy, Corros. Sci. 52 (2010) 1830–1837.
[10] H. Miao, H. Huang, Y. Shi, H. Zhang, J. Pei, G. Yuan, Effects of solution treatment before extrusion on the microstructure, mechanical properties and corrosion of Mg-Zn-Gd alloy in vitro, Corros. Sci. 122 (2017) 90–99.
[11] X.B. Chen, D.R. Nisbet, R.W. Li, P.N. Smith, T.B. Abbott, M.A. Easton, D.H. Zhang, N. Birbilis, Controlling initial biodegradation of magnesium by a biocompatible strontium phosphate conversion coating, Acta Biomater. 10 (2014) 1463–1474.
[12] X.B. Chen, X. Zhou, T.B. Abbott, M.A. Easton, N. Birbilis, Double-layered manganese phosphate conversion coating on magnesium alloy AZ91D: insights into coating formation, growth and corrosion resistance, Surf. Coat. Technol. 217 (2013) 147–155.
[13] X.B. Chen, N. Birbilis, T.B. Abbott, Effect of [Ca^{2+}] and [PO_4^{3-}] levels on the formation of calcium phosphate conversion coatings on die-cast magnesium alloy AZ91D, Corros. Sci. 55 (2012) 226–232.
[14] X.B. Chen, N. Birbilis, T.B. Abbott, A simple route towards a hydroxyapatite–Mg(OH)2 conversion coating for magnesium, Corros. Sci. 53 (2011) 2263–2268.
[15] H. Yang, X. Guo, G. Wu, W. Ding, N. Birbilis, Electrodeposition of chemically and mechanically protective Al-coatings on AZ91D Mg alloy, Corros. Sci. 53 (2011) 381–387.
[16] H. Yang, X. Guo, X. Chen, N. Birbilis, A homogenisation pre-treatment for adherent and corrosion-resistant Ni electroplated coatings on Mg-alloy AZ91D, Corros. Sci. 79 (2014) 41–49.
[17] S. Moon, Y. Nam, Anodic oxidation of Mg-Sn alloys in alkaline solutions, Corros. Sci. 65 (2012) 494–501.
[18] L. Hou, N. Dang, H. Yang, B. Liu, Y. Li, Y. Wei, X.B. Chen, A combined inhibiting effect of sodium alginate and sodium phosphate on the corrosion of magnesium alloy AZ31 in NaCl solution, J. Electrochem. Soc. 163 (2016) C486–C494.
[19] X. Liu, M. Yin, S. Zhang, H. Wei, B. Liu, H. Du, L. Hou, Y. Wei, Corrosion behavior of the as-cast and as-solid solution Mg-Al-Ge alloy, Materials 11 (2018).
[20] Y. Song, E.H. Han, D. Shan, C.D. Yim, B.S. You, The effect of Zn concentration on the corrosion behavior of Mg–xZn alloys, Corros. Sci. 65 (2012) 322–330.
[21] A. Pardo, M.C. Merino, A.E. Coy, F. Viejo, R. Arrabal, S. Feliú, Influence of microstructure and composition on the corrosion behaviour of Mg/Al alloys in chloride media, Electrochim. Acta 53 (2008) 7890–7902.
[22] J.L. Zhang, Y.L. Liu, J. Zhou, Z.Y. Feng, S.B. Wang, Kinetic study on the corrosion behavior of AM60 magnesium alloy with different Nd contents, J. Alloy. Comp. 629 (2015) 290–296.
[23] J.Y. Choi, W.J. Kim, Significant effects of adding trace amounts of Ti on the microstructure and corrosion properties of Mg-6Al-1Zn magnesium alloy, J. Alloy. Comp. 614 (2014) 49–55.
[24] G.L. Song, A. Ataens, X.L. Wu, B. Zhang, Corrosion behaviour of AZ21, AZ501 and AZ91 in sodium chloride, Corros. Sci. 40 (1998) 1769–1791.
[25] J. Yang, C.D. Yim, B.S. You, Effects of Sn in α-Mg matrix on properties of surface films of Mg-xSn (x = 0, 2, 5 wt%) alloys, Mater. Corros. 67 (2016) 531–541.
[26] J.W. Chang, P.H. Fu, X.W. Guo, L.M. Peng, W.J. Ding, The effects of heat treatment and zirconium on the corrosion behaviour of Mg–3Nd–0.2Zn–0.4Zr (wt.%) alloy, Corros. Sci. 49 (2007) 2612–2627.
[27] S. Candan, M. Unal, E. Koc, Y. Turen, E. Candan, Effects of titanium addition on mechanical and corrosion behaviours of AZ91 magnesium alloy, J. Alloy. Comp. 509 (2011) 1958–1963.
[28] R. Arrabal, A. Pardo, M.C. Merino, M. Mohedano, P. Casajús, K. Paucar, G. Garcés, Effect of Nd on the corrosion behaviour of AM50 and AZ91D magnesium alloys in 3.5 wt.% NaCl solution, Corros. Sci. 55 (2012) 301–312.
[29] M. Suresh, A. Srinivasan, K.R. Ravi, U.T.S. Pillai, B.C. Pai, Influence of boron addition on the grain refinement and mechanical properties of AZ91 Mg alloy, Mater. Sci. Eng. A 525 (2009) 207–210.
[30] J. Zhang, J. Wang, X. Qiu, D. Zhang, Z. Tian, X. Niu, D. Tang, J. Meng, Effect of Nd on the microstructure, mechanical properties and corrosion behavior of die-cast Mg–4Al-based alloy, J. Alloy. Comp. 464 (2008) 556–564.
[31] J. Zhang, X. Niu, X. Qiu, K. Liu, C. Nan, D. Tang, J. Meng, Effect of yttrium-rich misch metal on the microstructures, mechanical properties and corrosion behavior of die cast AZ91 alloy, J. Alloy. Comp. 471 (2009) 322–330.
[32] W. Liu, F. Cao, L. Zhong, L. Zheng, B. Jia, Z. Zhang, J. Zhang, Influence of rare earth element Ce and La addition on corrosion behavior of AZ91 magnesium alloy, Mater. Corros. 60 (2009) 795–803.
[33] Y. Fan, G. Wu, C. Zhai, Influence of cerium on the microstructure, mechanical properties and corrosion resistance of magnesium alloy, Mater. Sci. Eng. A 433 (2006) 208–215.
[34] N. Birbilis, G. Williams, K. Gusieva, A. Samaniego, M.A. Gibson, H.N. McMurray, Poisoning the corrosion of magnesium, Electrochem. Commun. 34 (2013) 295–298.
[35] W. Xu, N. Birbilis, G. Sha, Y. Wang, J.E. Daniels, Y. Xiao, M. Ferry, A high-specific-strength and corrosion-resistant magnesium alloy, Nat. Mater. 14 (2015) 1229–1235.
[36] L. Hou, M. Raveggi, X.B. Chen, W. Xu, K.J. Laws, Y. Wei, M. Ferry, N. Birbilis, Investigating the passivity and dissolution of a corrosion resistant Mg-33at.%Li alloy in aqueous chloride using online ICP-MS, J. Electrochem. Soc. 163 (2016) C324–C329.
[37] E. Brandes, G. Brook, Smithells Metals Reference Book, Butterworth-Heinemann, 1983.
[38] H. Men, Z. Fan, Effects of solute content on grain refinement in an isothermal melt, Acta Mater. 59 (2011) 2704–2712.
[39] M. Ascencio, M. Pekguleryuz, S. Omanovic, Corrosion behaviour of polypyrrole-coated WE43 Mg alloy in a modified simulated body fluid solution, Corros. Sci. 133 (2018) 261–275.
[40] Y. Song, D. Shan, R. Chen, E.-H. Han, Corrosion characterization of Mg–8Li alloy in NaCl solution, Corros. Sci. 51 (2009) 1087–1094.
[41] M.C. Reboul, P.H. Gimenez, J.J. Rameau, A Proposed Activation Mechanism for Al Anodes, Corrosion, 1984, pp. 366–371.
[42] A.G. Muñoz, S.B. Saidman, J.B. Bessone, Corrosion of an Al–Zn–In alloy in chloride media, Corros. Sci. 44 (2002) 2171–2182.
[43] N. Wang, R. Wang, C. Peng, B. Peng, Y. Feng, C. Hu, Discharge behaviour of Mg-Al-Pb and Mg-Al-Pb-In alloys as anodes for Mg-air battery, Electrochim. Acta 149 (2014) 193–205.
[44] I. Smoljko, S. Gudić, N. Kuzmanić, M. Kliškić, Electrochemical properties of aluminium anodes for Al/air batteries with aqueous sodium chloride electrolyte, J. Appl. Electrochem. 42 (2012) 969–977.
[45] A. Zazoua, N. Azzouz, An investigation on the use of indium to increase dissolution of AlZn anodes in sea water, Mater. Des. 29 (2008) 806–810.
[46] P. Gore, S. Fajardo, N. Birbilis, G.S. Frankel, V.S. Raja, Anodic activation of Mg in the presence of In^{3+} ions in dilute sodium chloride solution, Electrochim. Acta 293 (2019) 199–210.
[47] J. Li, B. Zhang, Q. Wei, N. Wang, B. Hou, Electrochemical behavior of Mg-Al-Zn-In alloy as anode materials in 3.5 wt.% NaCl solution, Electrochim. Acta 238 (2017) 156–167.
[48] H.Y. Ha, J.Y. Kang, J. Yang, C.D. Yim, B.S. You, Role of Sn in corrosion and passive behavior of extruded Mg-5 wt%Sn alloy, Corros. Sci. 102 (2016) 355–362.
[49] J. Yang, C.D. Yim, B.S. You, Characteristics of surface films formed on Mg-Sn alloys in NaCl solution, J. Electrochem. Soc. 163 (2016) C395–C401.
[50] T.W. Cain, C.F. Glover, J.R. Scully, The corrosion of solid solution Mg-Sn binary alloys in NaCl solutions, Electrochim. Acta 297 (2019) 564–575.